Anal Bioanal Chem (2003) 376 : 594–601
DOI 10.1007/s00216-003-1976-0

SPECIAL ISSUE PAPER

C. Riekel · M. C. García Gutiérrez · A. Gourrier · S. Roth

Recent synchrotron radiation microdiffraction experiments on polymer and biopolymer fibers

Received: 21 January 2003 / Revised: 6 April 2003 / Accepted: 14 April 2003 / Published online: 11 June 2003

Abstract The status of synchrotron radiation (SR) microdiffraction techniques developed at the ID13 beamline of the European Synchrotron Radiation Facility (ESRF) is reviewed for polymer and biopolymer fiber applications. Beam sizes in the micrometer-range have been used to study the local structure of whole fibers such as viscose-rayon or poly(p-phenylene terephthalamide). The possibilities for in situ studies during stretching, extrusion, or indentation will be discussed.

Introduction

X-Ray diffraction (XRD) techniques such as wide-angle X-ray scattering (WAXS) and small-angle X-ray scattering (SAXS) can be used to study structural order in semicrystalline polymer and biopolymer fibers from the unit cell to the mesoscale level (roughly up to 1 μm [1, 2, 3]. Beam sizes available from laboratory X-ray sources are usually in the range of 100 μm) or larger and therefore limit local area experiments. Microbeam XRD (μXRD) techniques developed at the microfocus beamline (ID13) of the ESRF are an extension of techniques developed at the Hasylab A2-beamline towards smaller beam sizes [4]. Beam sizes routinely available are in the range of 1–5 μm but are evolving to the sub-μm range [5].

The present article will review techniques developed for μXRD experiments on single polymer and biopolymer fibers. An overview is given on optics and instrumentation followed by an introduction to techniques for studying skin-core structures. The evolution of axial orientation during in situ experiments on fibers is discussed. Experiments on plastic deformation during indentation and bending of fibers are described. The necessity for sub-μm beams is shown for the example of kink band formation in an ultrahigh molecular weight polyethylene (UHMW-PE) fiber.

C. Riekel (✉) · M. C. García Gutiérrez · A. Gourrier · S. Roth
European Synchrotron Radiation Facility,
B.P. 220, 38043 Grenoble Cedex, France
e-mail: riekel@esrf.fr

Synchrotron radiation optics and instrumentation

The ESRF is a 3rd generation, brilliance optimized synchrotron radiation source. The characteristics of such sources are discussed in [6]. A schematic picture of the ID13 beamline is shown in Fig. 1A [5]. The SR-beam from an undulator radiation source is monochromatized by a Si-111 crystal and condensed to about 30 μm at the sample position by a mirror. The minimum distance of the first optical element to the source (here, monochromator at ≈29 m) is limited by the shielding wall of the storage ring. The X-ray beam size and divergence can be described by Gaussian profiles. Full-width-half-maximum (fwhm) values for the X-ray beam parameters at the source point (center of undulator) and the mirror focus (34.1 m from the source point) are indicated in Fig. 1A. For further beam size reduction add-on optics such as collimators or capillaries are placed into the focused beam [5, 7, 8]. μXRD techniques are currently routinely employing beam sizes of a few μm for polymer sample thicknesses down to a few μm. Sub-μm beams, are, however, becoming available and ≤100 nm beams have been reported [9, 10, 11]. Those techniques usually require little preparation of the sample, in contrast with transmission electron diffraction/imaging (TED/TEM) techniques which provide beam sizes down to about 10 nm but require elaborate embedding and sectioning techniques [12, 13].

Scanning μXRD experiments (S-μXRD) are usually done in transmission geometry by rastering the sample through the beam and recording a difffraction pattern after every step using a charge-coupled-device (CCD) detector. The scanning set-up shown in Fig. 1B allows optimization of the beam at the sample position for minimum size (WAXS-applications:[5]) or minimum divergence (SAXS-applications:[8]) by using different add-on optics. The sample is initially examined off-axis from the beam by a long-distance microscope and a region of interest (ROI) is se-

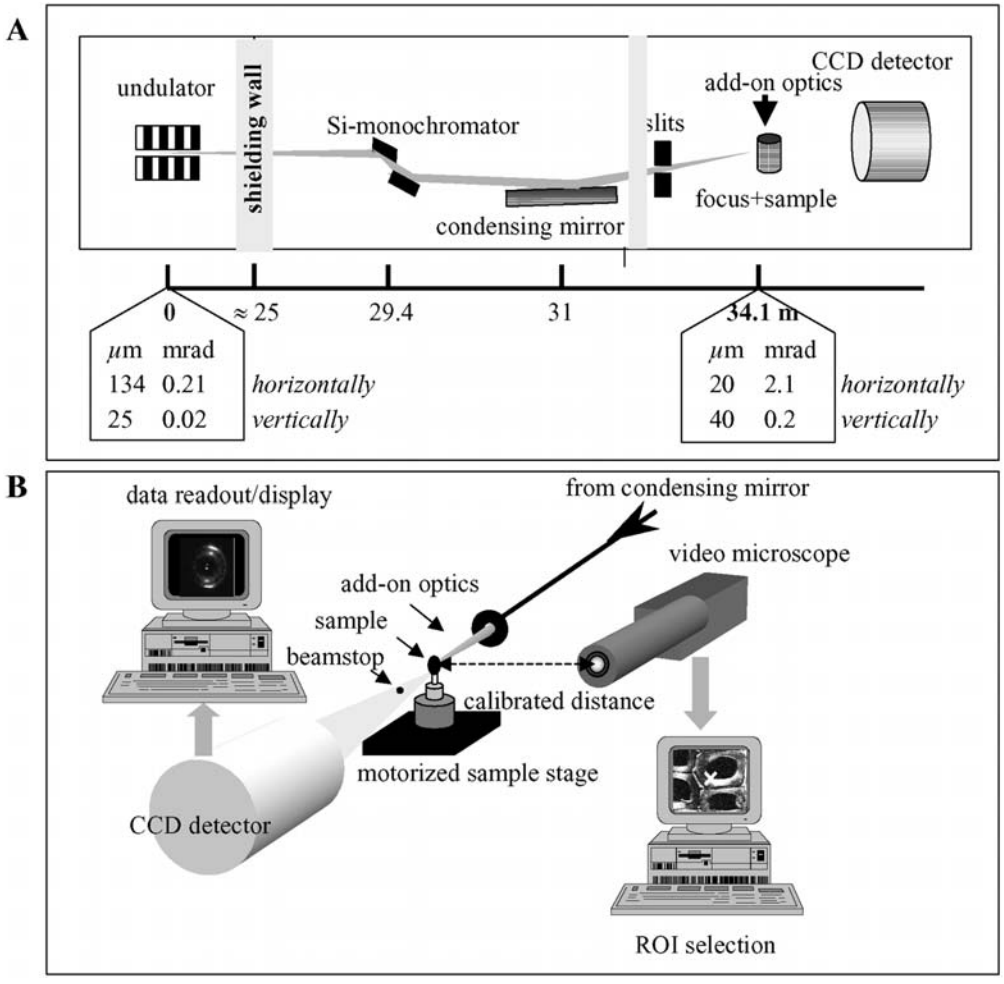

Fig. 1 **A** Schematic layout of the ESRF ID13 beamline [5]. The size (µm, fwhm) and the divergence (mrad, fwhm) of the beam at the undulator source point (0 m) and at the focus of the condensing mirror (34.1 m) are indicated for the vertical and horizontal directions. **B** Schematic design of S-µXRD scanning set-up [5]. The region of interest (ROI) to be scanned is selected by a video microscope and transferred into the beam by a motorized stage. A 1D or 2D raster-scan of the ROI through the beam is then performed and a µXRD-pattern is recorded after every raster step

lected for scanning. The ROI is then transferred by a motorized gantry into the beam and the raster parameters for a linear (1D) or area (2D) scan are chosen. Details of the data analysis and interpretation will not be discussed in this review.

Selected applications

Local fiber structures

Semicrystalline polymeric fibers can be modeled as fibrillar systems organized on many length scales starting from the atomic level [14]. XRD experiments on fibers are often interpreted in terms of scattering from a distribution of (coherently scattering) crystalline blocks, which constitute the microfibrils [12, 15]. Those blocks are assumed to be randomly oriented around the fiber axis. As the crystalline block sizes are usually in the range of a few nm one can assume that local fiber symmetry is maintained for µXRD beam sizes in the µm and sub-µm range. Examples studied are viscose-rayon [16] or high performance fibers such as carbon fibers [17, 18], poly(p-phenylene terephthalamide) (PPTA, brand names: Kevlar, Twaron) [19], UHMW-PE [20], and poly(p-phenylene benzobisoxazole) (PBO) [21].

Many fibers contain skin layers, which differ from the bulk by the size or orientation distribution of the crystalline blocks. Such morphological differences are best examined for a beam size, which is significantly smaller than the diameter of the fiber. Thus, Fig. 2A shows a transmission electron microscopy (TEM) image of a longitudinal cross-section (100 nm thick) of a 9 µm diameter viscose-rayon fiber [16]. The core region appears to be slightly darker than the skin-region. The transmission electron diffraction (TED) patterns of the skin and core regions were obtained from a 1 µm diameter area. An improvement in the orientation of the crystalline blocks along the fiber axis in the skin-region is qualitatively indicated by a more narrow azimuthal intensity distribution of the equatorial reflections. Figure 2B shows a scanning electron microscopy (SEM) image of a single fiber. S-µXRD patterns have been obtained with a 2 µm beam from the skin and center (skin+core pattern). The core-pattern has been derived by subtracting the skin-pattern from the pattern recorded at the center of the fiber. The skin-pattern shows again a narrower crystalline block orientation distribution in the skin.

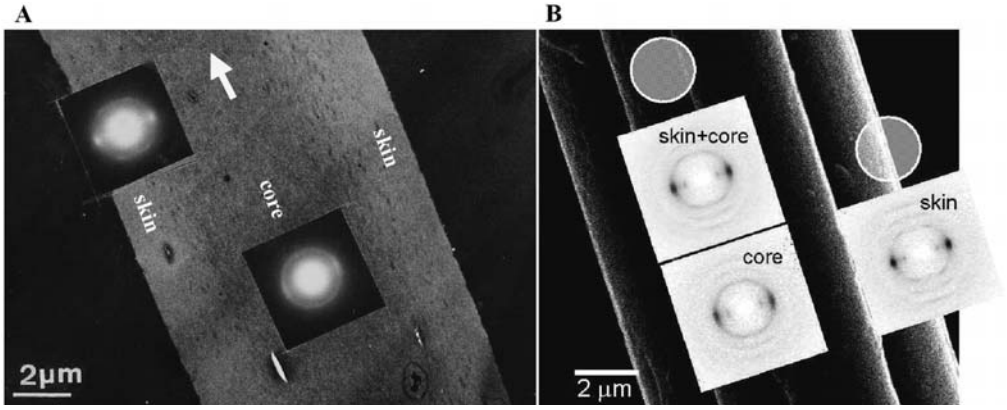

Fig. 2 **A** Transmission electron microscopy (TEM) image of a 100 nm-thick longitudinal section of a viscose-rayon fiber with overlaid transmission electron diffraction (TED) patterns from skin and core zones [16]. The direction of the fiber axis is indicated by an *arrow*. The TED patterns were obtained from a 1 µm diameter area. **B** SEM picture of single viscose-rayon fiber with overlaid µXRD patterns of skin, skin+core, and core zones. The core pattern was obtained by subtracting the skin contribution from the skin+core pattern. The size of the X-ray beam is indicated by a *white circle*

The orientation distribution of crystalline blocks along the fiber axis is often quantified in terms of Herman's orientation function [22]:

$$f_c = 0.5\left[3 < \cos^2 \phi > -1\right] \quad (1)$$

The average angle of crystalline block orientation along the fiber axis (<cos²φ>) can be derived from the azimuthal spread of meridional (along fiber axis) or equatorial (normal to fiber axis) reflections. A single diffraction pattern is sufficient for this analysis provided that the assumption of fiber symmetry holds [22]. Thus, Fig. 3A shows the fiber diffraction pattern from a single Kevlar[29] fiber of 12 µm diameter obtained with a 3 µm beam. The variation of the orientation function shown in Fig. 3B has been derived from the 110/200 reflections recorded during a raster-scan ($2_{hor}\times5_{vert}$ µm steps). In this case a gradient in orientation function from the skin to the core was observed [19]. By averaging the local f_c-values for the PPTA-brands Kevlar[x] (x:29, 49, 149) obtained in this way one obtains f_c-values which are in good agreement with single fiber f_c-values obtained with a larger X-ray beam [23]. The skin-core morphology of viscose-rayon fibers could be quantified in the same way by a linear scan across the fiber [16].

Stretching experiments

Deformation and heat treatment are the most common methods to obtain an improvement of the mechanical properties of a fiber. Thus, a proprietary process is used to improve Young's modulus in the series Kevlar[x] (x:29, 49, 149). This is linked with an improvement of the orientation function as can be demonstrated for an in situ stretching experiment on a Kevlar[29] fiber [19]. The micro-stretching cell shown in Fig. 4A can be used to raster-scan a single fiber with an about 3 µm spot generated by a glass capillary during stretching. As shown in Fig. 4B, the gradient in orientation function derived from such experiments disappears at an applied force of about 1.5 GPa [19].

The same techniques have been applied to investigate crystalline block orientation during the extrusion of silk from the spigots (exit of the spinnerets) of living orb-weaving spiders [24, 25, 26]. The technical challenges are (i) single silk fiber diameters of <5 µm, (ii) low volume

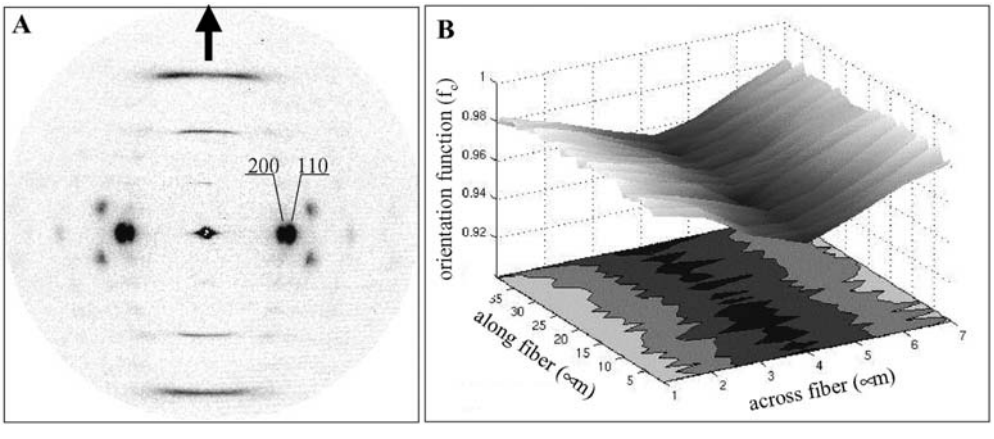

Fig. 3 **A** Single fiber diffraction pattern from the center of a 12 µm diameter Kevlar fiber recorded with a 3 µm X-ray beam. The direction of the fiber axis (meridian) is indicated by an *arrow*. **B** Variation of Herman's orientation function (f_c) across a Kevlar[29] fiber (see text). The data were obtained from a raster-scan ($2_{hor}\times5_{vert}$ µm steps)

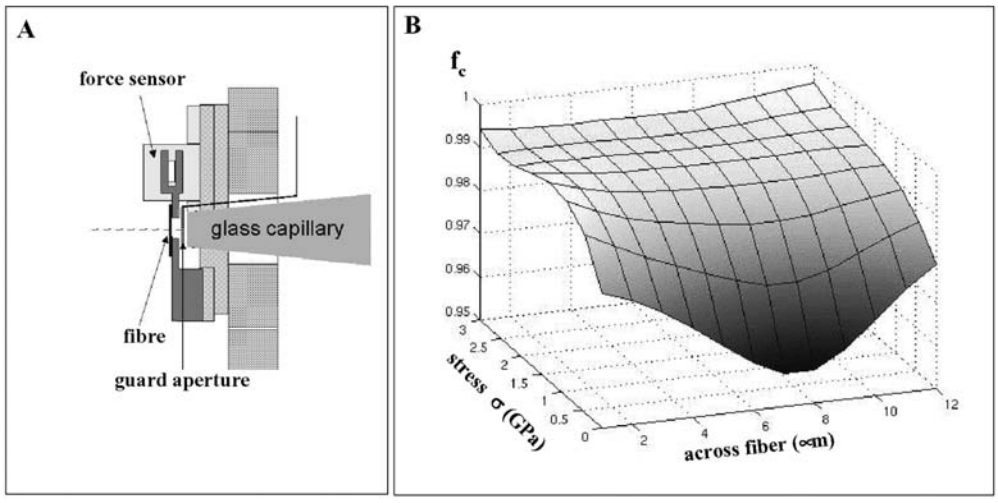

Fig. 4 **A** Micro-stretching cell for S-µXRD with beam defining glass capillary [19]. A guard aperture reduces background scattering from the capillary exit. The fiber is glued to a force sensor, which allows measurement of the stress variation during stretching. **B** Variation of f_c-gradient across the Kevlar[29] fiber during stretching. The raster-scan corresponds to that shown in Fig. 3B but the patterns for every stress-level have been averaged along the vertical (fiber) axis

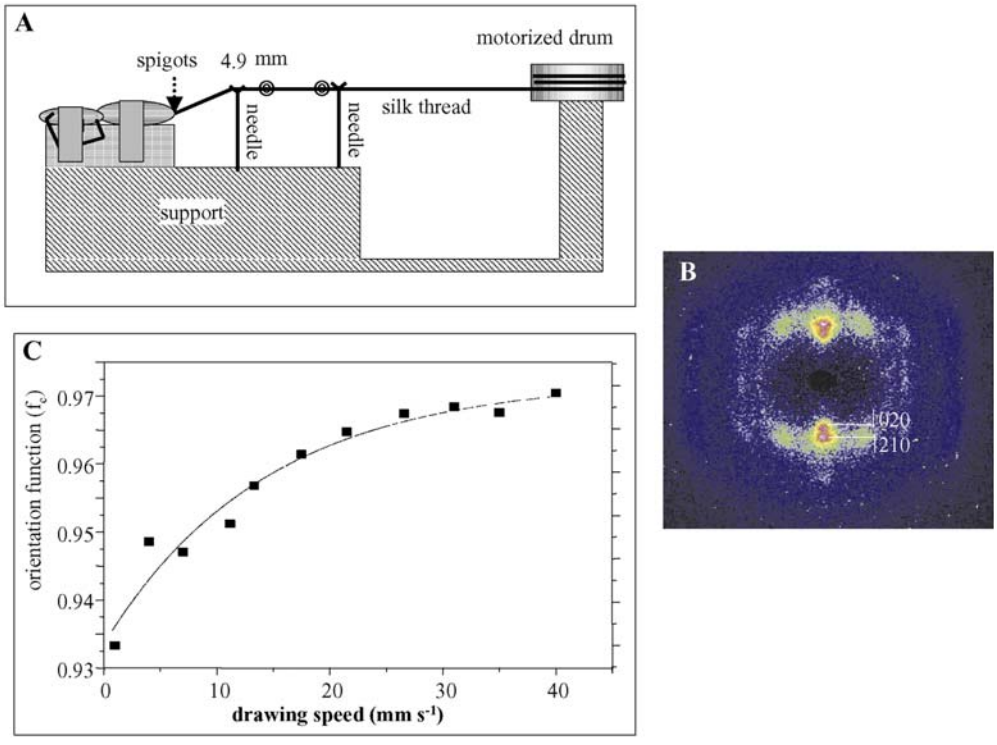

Fig. 5 **A** In situ extrusion set-up for forced silking of orb-weaving spiders [25]. The spider is fixed to the support structure by Mylar taps. The silk thread is extracted from the spigots by the forced silking technique [29] using a motorized drum and two guiding needles. **B** Single fiber pattern recorded at 4.9 mm from the spigots. Note that the meridional axis is horizontal. **C** Variation of Herman's orientation function (f_c) as a function of drawing speed [25]. The extrusion speed during natural web building activity is a few mm s^{-1}. Dragline production can result in much higher extrusion speeds (100 mm s^{-1} or more) [45]

crystallinity of <30% [27] and (iii) the movement of the spigots due to biological activity [28]. The set-up shown in Fig. 5A allows drawing a single silk fiber or a thread (two fibers) from the spigots at a controlled speed using a motorized drum by the so-called forced silking technique [29]. The silk fiber is stabilized in position by guiding needles so that S-µXRD patterns can be recorded with a 10 µm beam [25, 26]. Radiation damage can be neglected as the sample is continuously moved through the beam during exposure. A single pattern obtained at 4.9 mm from the spigots corresponds to the β(poly-L-alanine) structure [30] (Fig. 5B). The variation of the orientation function determined as a function of drawing rate from the 020/210 reflections (Fig. 5C) suggests a post-drawing process improving crystalline block orientation and is in good agreement with the increase of drawing stress with drawing speed [31].

Plastic deformation

Microindentation is often used as a measure to determine the hardness of polymeric materials [32] (Fig. 6A). The impression remaining in a polymer after microindentation is mainly due to plastic deformation although the nature and extent of microscopic processes is not directly accessible to laboratory XRD techniques. Structural processes occurring below a diamond indenter tip (Vickers type [32])

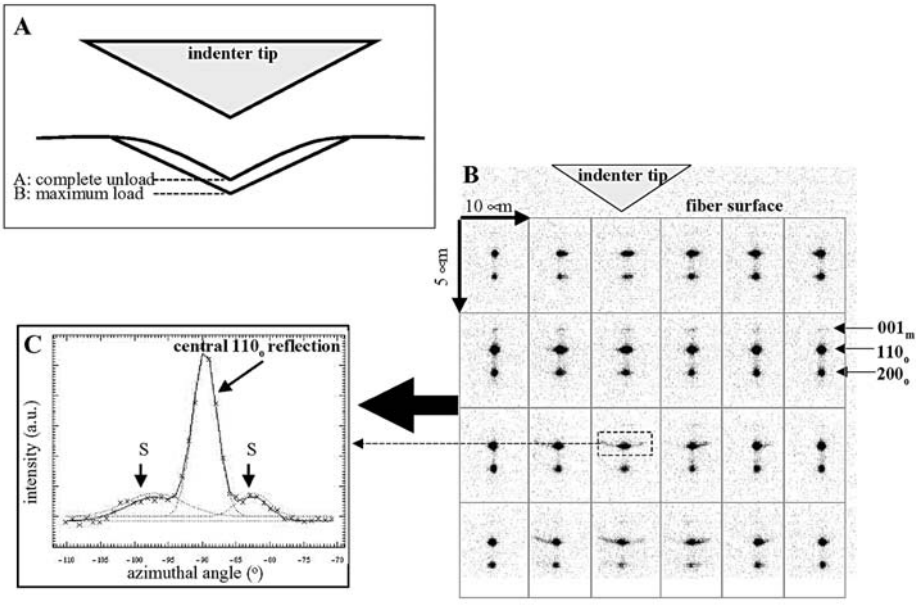

Fig. 6 **A** Schematic picture of an indentation experiment. The indenter tip is deforming the material up to maximum load. The remaining impression after complete unload is due to plastic deformation. **B** Composite image obtained from a raster-scan ($10_{hor}\times5_{vert}$ µm steps) of the indented zone in a UHMW-PE fiber. The "pixels" of the composite image are limited to selections containing the $110_0/200_0$ and 001_m reflections (see text). The macroscopic fiber axis is indicated by an *arrow*. **C** The azimuthal profile of a specific 110_0 reflection can be fitted by two Gaussian functions corresponding to a central and two satellite peaks (S) and a linear background. The fitting method is explained in [35]. The *second row from top* shows the 001_m reflection of the monoclinic phase in addition to the orthorhombic phase reflections ($110_o/200_o$)

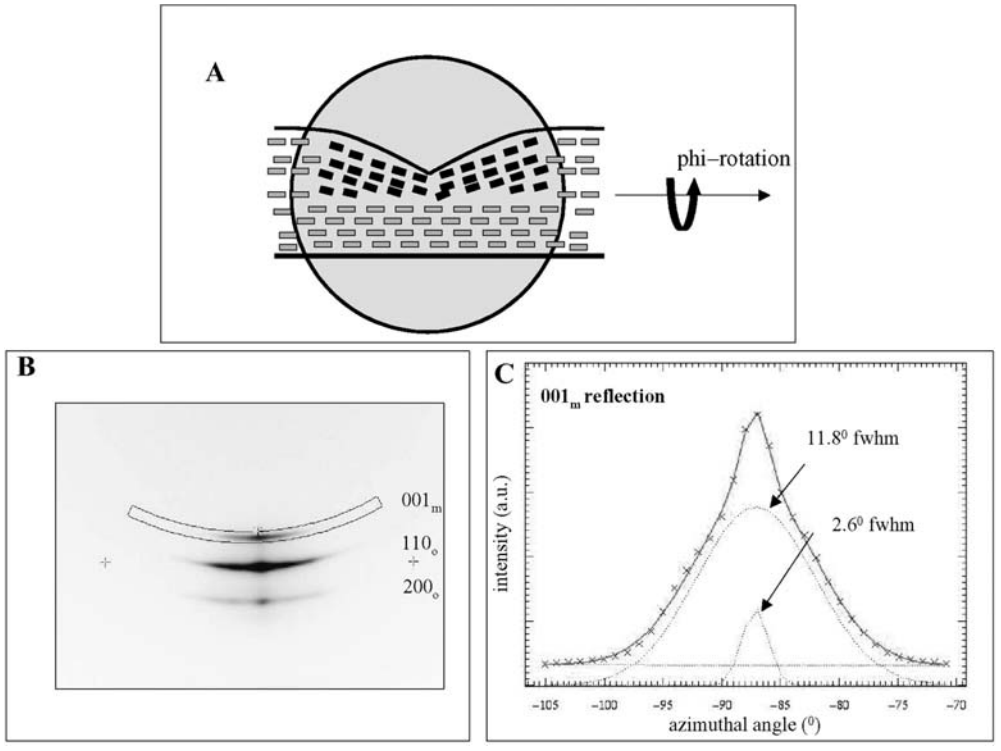

Fig. 7 **A** Idealized model of indented fiber. The arrangement of the crystalline blocks in the undeformed zone (*light gray*) correspond to a fiber texture. Chain-interconnects between the blocks (tie-molecules) are omitted. Two domains of crystalline blocks in the plastically deformed zone (*dark*) are formed due to the indenter tip strain field. The X-ray beam is indicated schematically by a *circle*. **B** Equatorial reflections of the indented fiber using a 30 µm diameter beam (*left*). The intensity of the 001_m reflection was summed radially and the corresponding azimuthal intensity distribution is shown to the *right*. Two Gaussian functions with 2.6° fwhm and 11.8° fwhm were fitted to the intensity distribution

have, however, been examined using a dedicated S-µXRD set-up in such samples as isotactic polypropylene (iPP), Nylon 66, and UHMW-PE [33, 34]. Figure 6B shows an image based on a raster-scan ($10_{hor}\times5_{vert}$ µm steps, 5 µm beam) of a 12 µm diameter UHMW-PE fiber after it had been indented with a force of 10 mN [35]. The image is composed of selections of an area of the diffraction pattern, each containing the same part of the equator at the different points of the scan. The macroscopic fiber axis is depicted by an arrow. The impact point of the indenter on the fiber is shown schematically.

The stable form of PE has an orthorhombic structure with the two strongest equatorial reflections, 110_o and 200_o [2]. However, the 2nd row from the top in Fig. 6B shows, in addition, the presence of the metastable monoclinic PE-phase via its 001_m reflection. The 3rd row shows the formation of satellite reflections to the 110-peak. The impact point of the indenter on the fiber can be easily recognized via a symmetric satellite peak separation on the azimuth which is shown in more detail in Fig. 6C for a specific image selection. The satellite peaks reflect the formation of two domains due to the strain field of the in-

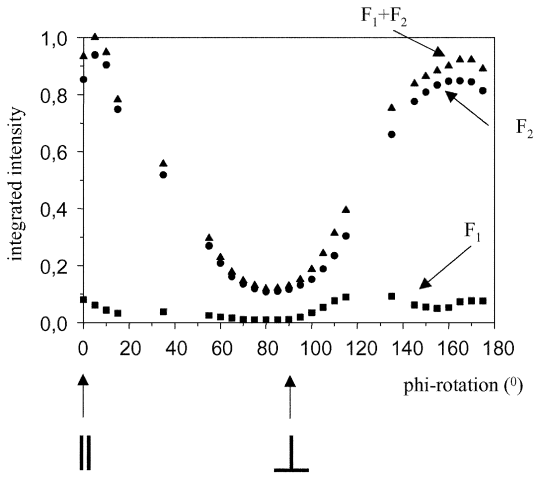

Fig. 8 Variation of relative integrated intensities of narrow (F_2) and broad (F_1) peaks (Fig. 7B) as a function of the rotation angle phi. The X-ray beam is parallel to the indentation direction at phi=0° and normal at phi=90°. The intensities were scaled to 1.0 for the maximum intensity of the sum F_1+F_2

denter tip acting normal to the fiber direction [35]. The deformation field of the indenter tip entering the fiber induces, therefore, first a partial phase transformation followed by an irreversible breaking up into domains, which corresponds to the plastic deformation process. These domains are shown schematically in Fig. 7A surrounded by crystalline blocks with a fiber orientation distribution. The plastic deformation also induces, however, an alignment of the crystalline blocks in the direction of the deformation field [34]. The alignment can be verified by rotating the fiber around an axis normal to the beam direction (phi-axis) in 5° steps and recording during every step a diffraction pattern. The experiment is performed with a beam of 30 µm diameter which covers completely the deformed zone plus a fraction of undeformed fiber.

For the model of a random orientation of crystalline blocks around the fiber axis the [110_o] and [100_o] axes are statistically distributed normal to the fiber axis. An analysis of the preferred orientation of the (110_o) or (100_o) planes would require a separation of the deformed and undeformed fractions which is not straightforward. The [001_m] axis is, however, also oriented normal to the [001_o] axis [2]. An analysis of the (001_m) planes allows neglection of the fraction of undeformed material present in the beam since the amount of monoclinic phase present in the

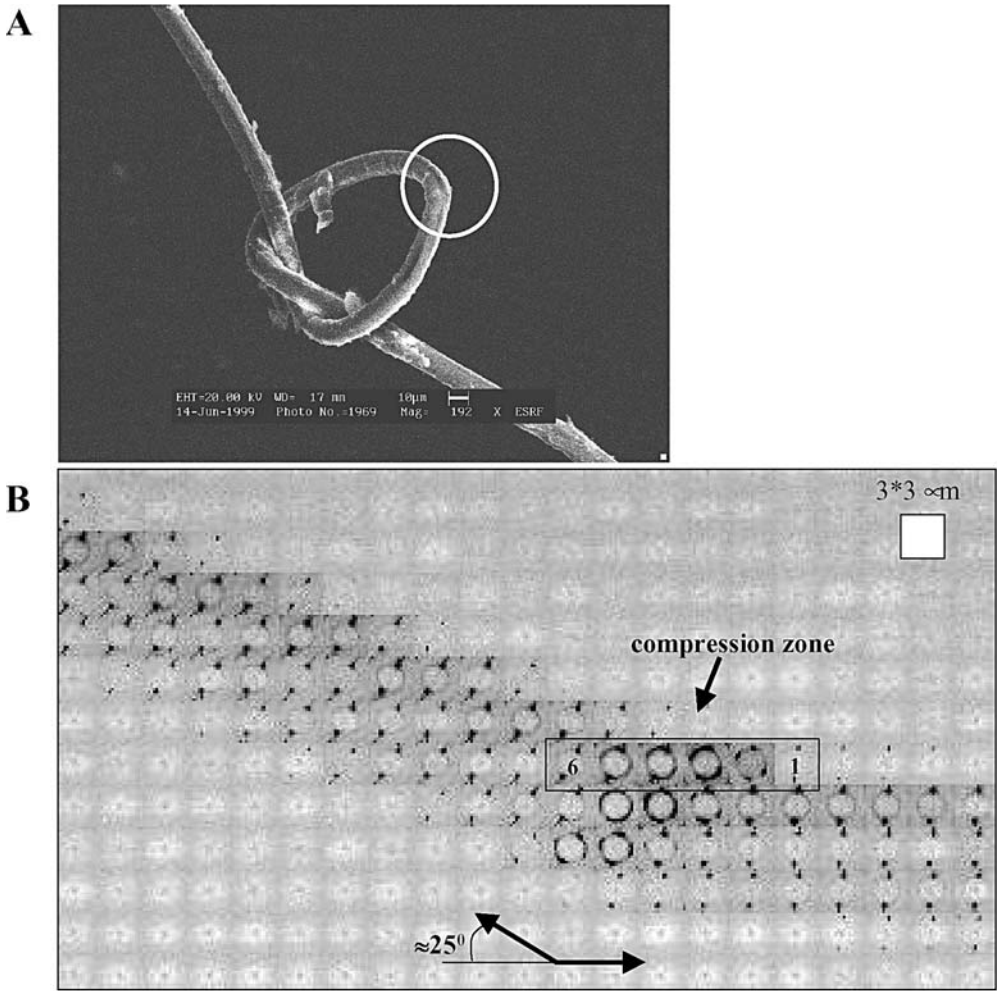

Fig. 9 **A** Knot in UHMW-PE fiber imaged by SEM. The *circle* indicates a kink band zone. **B** S-µXRD raster-scan (3_{hor}×3_{vert} µm steps, 3 µm beam) of the kink band zone indicated in Fig. 9A. The "pixels" of the composite image show selections containing the strongest equatorial reflections. The *arrows* indicate the orientations of the fiber axes outside of the kink band zone

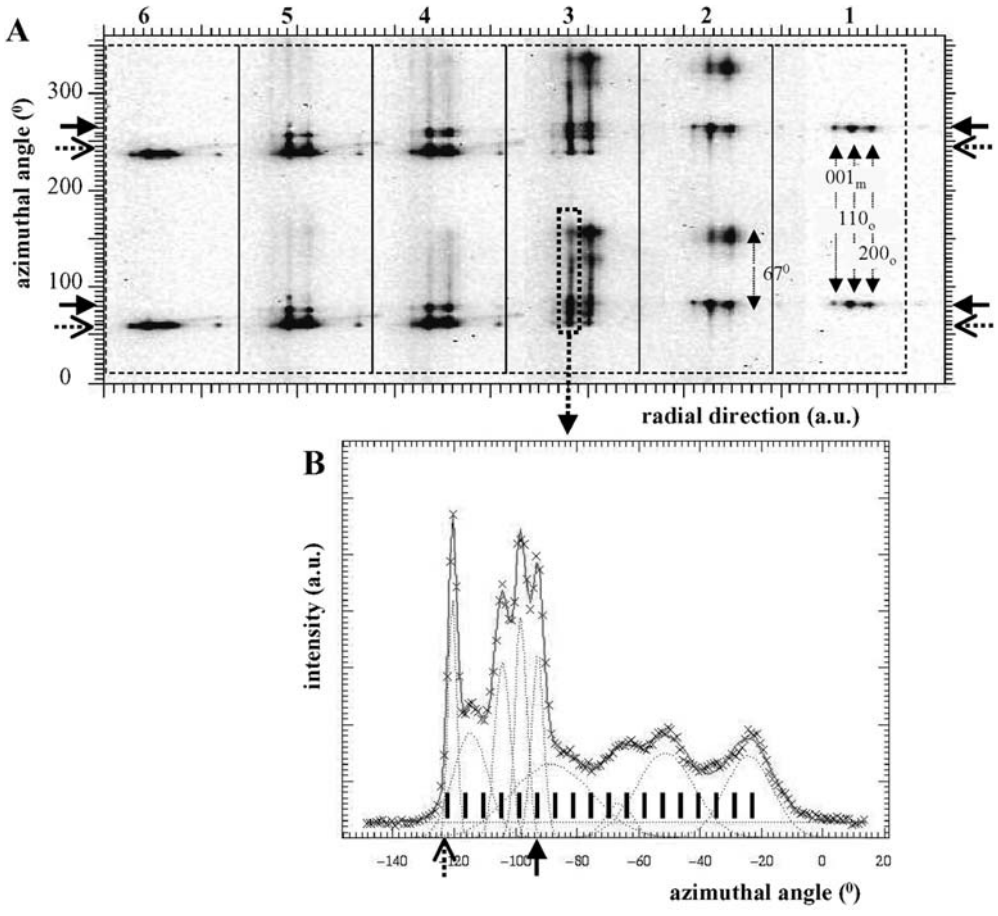

Fig. 10 **A** Angularly regrouped patterns (1–6) from the compression zone shown in Fig. 9B. The azimuthal angle corresponds to the ordinate while the abscissae corresponds to the radial direction. The picture is composed out of "pixels" corresponding to selections shown in Fig. 9B. The azimuthal orientation of the equator outside the bent zone is indicated by *arrows*. **B** Azimuthal intensity profile (*crosses*) at the (radial) 110_o position. The fitted curve (*solid line*) is composed of nine Gaussian functions. Note that the azimuthal scale is not the same as in Fig. 10.A. The hypothetical grid has been calculated for an average kink separation of 5.7°

undeformed material is very small. Figure 7B shows the angular range over which the 001_m reflection was radially integrated. The azimuthal intensity distribution (Fig. 7C) can be separated by two Gaussian functions into a narrow peak (F_1-fraction) and a broad peak (F_2-fraction). (Fig. 7C) The minor, F_1-fraction (2.6° fwhm) is assigned to a fraction already present in virgin material, which has probably been formed during the extrusion process [20] while the F_2 fraction has been formed during the indentation process. Figure 8 shows the strong orientational texture of the F_2-fraction while the F_1-fraction is practically not affected. Models for the mechanism of plastic deformation in terms of a transverse slip system, which have been developed for PE [36, 37], might also apply to this indentation experiment.

Plastic deformation is also present in a fiber which has been bent beyond its elastic limit as shown for the knot in an UHMW-PE fiber (Fig. 9A, circled zone). The bent zone is characterized by the formation of kink bands [38, 39] which should result in discrete changes of the local fiber axis orientation across the deformed zone. The composite image based on a raster-scan ($3_{hor}\times3_{vert}$ µm steps, 3 µm beam) across the deformed zone (Fig. 9A) shows that the macroscopic fiber axis changes its direction by about 25° (Fig. 9B). A sequence of six angular regrouped patterns from the compression zone indeed indicates a discontinuous fiber axis reorientation associated with diffuse scattering (Fig. 10A). Pattern no. 1 corresponds to the undeformed fiber with some monoclinic phase. Deformation starts in pattern no. 2 by a doubling of the equatorial pattern. The angle of 67° between the equatorial patterns agrees to a {110} twinning process which has been termed mechanical twinning. [40, 41, 36] The fiber orientation at about 25° to the pattern no. 1 appears in pattern no. 3 together with a sequence of azimuthal peaks connecting the principal equatorial patterns. A fit of nine Gaussian functions can describe the azimuthal profile at the position of the 110_o peak in this pattern quite well (Fig. 10B). One notes the presence of narrow (≈2° fwhm) and broad (>5° fwhm) peaks. The narrow peaks are tentatively assigned to multiple kinks where the lattice rotates at every step by about 5.6°. It is, however, possible that the beam size was not sufficient to resolve such kinks for the broader peaks. Based on the angular separation of the narrow peaks one could thus calculate the angular position of the individual kinks as shown by the grid in Fig. 10B. The intensity oscillation might be related to the scattering volume of the individual kinks within the volume sampled by the beam. This example shows that smaller beam sizes will be required to verify such a model. Current limitation for S-µXRD experiment are for about 100 nm beams [42]. As the formation of such kinks is not well understood [43] it would also be very interesting to perform in situ studies with a fiber bender developed for Raman spectroscopy [44].

Conclusions

S-μXRD techniques reviewed in this article can be routinely applied to a large range of polymeric and biopolymeric samples. These techniques are particularly complimentary to EM/ED techniques for in situ applications. Evidently S-μXRD techniques can also be applied to other materials. An extension to sub-μm beam sizes is required for applications involving fibers of less than 10 μm diameter, local defects, and fiber interfaces in composite materials.

Acknowledgements We wish to acknowledge the support during SR experiments by M. Burghammer. The use of glass capillary optics is based on a collaboration with P. Engström and A. Rindby (Chalmers). Spider spinning experiments are based on a collaboration with F. Vollrath et al. (Oxford University).

References

1. Guinier A (1955) Small-angle scattering of X-rays. Wiley, New York
2. Tadokoro H (1990) Structure of crystalline polymers. Krieger, Malabar
3. Glatter O (1982) In: Glatter O, Kratky O (eds) Small angle scattering. Academic Press, New York, p 119
4. Elsner G, Riekel C, Zachmann HG (1985) Synchrotron radiation in polymer science. In: Kausch HH, Zachmann HG (eds) Advances in polymer science. Springer, Berlin Heidelberg New York
5. Riekel C (2000) Rep Prog Phys 63:233–262
6. Raoux D (1993) In: Baruchel J et al (eds) Introduction to synchrotron radiation and to the physics of storage rings in Neutron and synchrotron radiation for condensed matter studies. Springer, Berlin Heidelberg New York, pp 37–78
7. Engström P, Riekel C (1996) Rev Sci Instr 67(12):4061–4063
8. Riekel C, Burghammer M, Müller M (2000) J Appl Cryst 33: 421–423
9. Jark W, DiFonzo S, Lagomarsino S, Cedola A, Fabrizio ED, Bram A, Riekel C (1996) J Appl Phys 80(9):4831–4836
10. Müller M, Burghammer M, Flot D, Riekel C, Morawe C, Murphy B, Cedola A (2000) J Appl Cryst 33:1231–1240
11. Pfeiffer F, David C, Burghammer M, Riekel C, Salditt T (2002) Science 297:230–234
12. Sawyer LC, Grubb DT (1996) Polymer microscopy. Chapman & Hall, London
13. Taylor JE, Romo-Uribe A, Libera MR (2002) Polymer 43:1641–1648
14. Baer E, Hiltner A, Keith HD (1987) Science 235:1015–1022
15. Smith P, Boudet A, Chanzy H (1985) J Mater Sci Lett 4:13–18
16. Müller M, Riekel C, Vuong R, Chanzy H (2000) Polymer 41(7): 2627–2632
17. Paris O, Loidl D, Mueller M, Lichtenegger H, Peterlik H (2001) J Appl Cryst 34:473–479
18. Lozano-Castello D, Raymundo-Pinero E, Cazorla-Amoros D, Linares-Solano A, Mueller M, Riekel C (2002) Carbon 40:2727–2735
19. Riekel C, Dieing T, Engström P, Vincze L, Martin C, Mahendrasingam A (1999) Macromolecules 32:7859–7865
20. Riekel C, Cedola A, Heidelbach F, Wagner K (1997) Macromolecules 30(4):1033–1037
21. Davies RJ, Montes-Moran MA, Riekel C, Young RJ (2001) J Mater Sci 36:3079–3087
22. Stein RS, Wilkes GL (1975) Physico-chemical approaches to the measurement of anisotropy. In: Ward IM (ed) Structure and properties of oriented polymers. Applied Science, London, pp 57–145
23. Wu TM, Blackwell J (1996) Macromolecules 29:5621–5627
24. Riekel C, Müller M, Vollrath F (1999) Macromolecules 32(13): 4464–4466
25. Riekel C, Madsen B, Knight D, Vollrath F (2000) Biomacromolecules 1:622–626
26. Riekel C, Vollrath F (2001) Int J Biol Macromol 29(3):203–210
27. Grubb DT, Jelinski LW (1997) Macromolecules 30(10):2860–2867
28. Foelix R (1996) Biology of spiders. Oxford University Press
29. Work RW, Emerson PD (1982) J Arachnol 10:1–10
30. Fraser RDB, MacRae TP (1973) Conformations of fibrous proteins. Academic Press, New York
31. Knight D, Knight M, Vollrath F (2000) Int J Biol Macromol 27(3):205–210
32. Baltá-Calleja FJ, Fakirov S (2000) Microhardness of polymers. Cambridge Solid State Science Series, Cambridge University Press, Cambridge
33. García-Gutiérrez MC, Gourrier A, Riekel C (2003) J Macromol Sci Phys (in press)
34. Gourrier A, García-Gutiérrez MC, Riekel C (2002) (unpublished)
35. Gourrier A, García-Gutiérrez MC, Riekel C (2002) Macromolecules 35(21):8072–8077
36. Lin L, Argon AS (1994) J Mater Sci 29:294–323
37. Galeski A, Bartczak Z, Argon AS, Cohen RE (1992) Macromolecules 25:5705-5718
38. Lemstra PJ, Kirschbaum R, Ohta, T, Yasuda H (1987) High-strength/high-modulus structures based on flexible macromolecules: gel-spinning and related processes. In: Ward IM (ed) Developments in orientated polymers. Elsevier, London, pp 39–77
39. Jiang H, Adams WW, Eby RK (1993) High performance polymer fibres. In: Cahn RW, Haasen P, Kramer EJ (eds) Materials science and technology. VCH, Weinheim, pp 597–652
40. Frank FC, Keller A, O'Connor A (1958) Phil Mag 8:64–74
41. Allan P, Crellin EB, Bevis M (1973) Phil Mag 27:127–145
42. Roth S, Burghammer M, Janotta A, Riekel C (2002) Macromolecules 36:1585–1593
43. Kozey VV, Jiang H, Mehta VR, Kumar S (1995) J Mater Res 10(4):1044–1061
44. Sirichaisit J, Young RJ (1999) Polymer 40:3421–3431
45 Vollrath F, Knight DP (2001) Nature 410:541–548